Wavefield interpolation in 3D large-step Fourier wavefield extrapolation

Gaoxiang Chen[1,3], Li-Yun Fu[1,2*], Wei Wei[1] and Weijia Sun[1]

[1]*Key Laboratory of Petroleum Resource Research, Institute of Geology and Geophysics, Chinese Academy of Sciences, Beijing 100029, China,* [2]*The State Key Laboratory of Ore Deposit Geochemistry, Institute of Geochemistry, Chinese Academy of Sciences, Guiyang 550081, China, and* [3]*Zhejiang Provincial Institute of Communication, Planning, Design and Research, Zhejiang 310000, China*

ABSTRACT

Extrapolating wavefields and imaging at each depth during three-dimensional recursive wave-equation migration is a time-consuming endeavor. For efficiency, most commercial techniques extrapolate wavefields through thick slabs followed by wavefield interpolation within each thick slab. In this article, we develop this strategy by associating more efficient interpolators with a Fourier-transform-related wavefield extrapolation method. First, we formulate a three-dimensional first-order separation-of-variables screen propagator for large-step wavefield extrapolation, which allows for wide-angle propagations in highly contrasting media. This propagator significantly improves the performance of the split-step Fourier method in dealing with significant lateral heterogeneities at the cost of only one more fast Fourier transform in each thick slab. We then extend the two-dimensional Kirchhoff and Born–Kirchhoff local wavefield interpolators to three-dimensional cases for each slab. The three-dimensional Kirchhoff interpolator is based on the traditional Kirchhoff formula and applies to moderate lateral velocity variations, whereas the three-dimensional Born–Kirchhoff interpolator is derived from the Lippmann–Schwinger integral equation under the Born approximation and is adapted to highly laterally varying media. Numerical examples on the three-dimensional salt model of the Society of Exploration Geophysicists/European Association of Geoscientists demonstrate that three-dimensional first-order separation-of-variables screen propagator Born–Kirchhoff depth migration using thick-slab wavefield extrapolation plus thin-slab interpolation tolerates a considerable depth-step size of up to 72 ms, eventually resulting in an efficiency improvement of nearly 80% without obvious loss of imaging accuracy. Although the proposed three-dimensional interpolators are presented with one-way Fourier extrapolation methods, they can be extended for applications to general migration methods.

Key words: 3D Fourier depth migration, First-order separation-of-variables screen propagator, Thick-slab extrapolation, Thin-slab interpolation, 3D Born–Kirchhoff interpolators.

INTRODUCTION

Fourier-transform-based migration methods have been widely used in seismic imaging because of their many desirable properties, including analytical wavefield extrapolation, algorithm simplicity, high computational efficiency with fast Fourier transforms (FFTs), amplitude preservation by honouring Snell's law naturally, and immunisation against both grid dispersion and operator splitting errors occurring in 3D cases.

*E-mail: lfu@mail.iggcas.ac.cn

In particular, Fourier wavefield extrapolation can tolerate a much larger depth-step size than conventional finite-difference (FD) wavefield extrapolation in the presence of lateral velocity variations and dipping events. This article develops supporting 3D wavefield interpolation techniques to image small layers inside excessively large depth intervals.

Early Fourier extrapolators present various difficulties in handling wide-angle propagations and lateral velocity variations simultaneously (Cheng, Cheng and Toksöz 1996; Huang and Fehler 1998). Several improvements have been achieved for this problem over the past few decades. For example, both the split-step Fourier (SSF) (Stoffa *et al.* 1990) and phase-screen propagators (Wu 1996) are suitable for either weak-contrast heterogeneities or small propagation angles. Slight modifications to the phase-screen propagator have lead to a category of pseudo screen propagators (Wu 1996; Huang, Fehler and Wu 1999), generalised screen propagators (de Hoop, Le Rousseau and Wu 2000; Le Rousseau and de Hoop 2001; Liu and Zhang 2006), and broadband constant-coefficient propagators (Fu 2005) for moderate laterally heterogeneous media. For large-contrast slabs with wide-angle propagations, the most appropriate method may be the first-order separation-of-variables screen propagator (SVSP1) (Fu 2006) formulated from the generalised Lippmann–Schwinger integral equation. Strong lateral velocity contrasts may be addressed by the multiple-reference-velocity Fourier method (Gazdag and Sguazzero 1984; Kessinger 1992), the windowed phase-screen method (Wu and Jin 1997), and the optimised Chebyshev–Fourier method (Zhang *et al.* 2010). These high-accuracy Fourier migration schemes are capable of simultaneously imaging steep dips and handling complex media with arbitrary velocity variations in all directions.

However, because of the multiple reference velocities used or high-order approximations to the one-way wave equation, these aforementioned Fourier migration methods require extra computations at each depth step, which increases the computational time considerably especially for immense 3D cases. In general, Fourier migration techniques for practical applications allow for the downward continuation of wavefields through thick slabs, with the depth-step size usually chosen to be several times as large as the output depth sampling interval. However, excessively coarse depth steps cause visible spurious kinks along dipping reflectors in the migration section. Although eliminating these kinks is possible by using proper interpolators inside each thick slab, the results are severely affected by the characteristics of the interpolator used. Fu (2004) proposed three 2D interpolation algorithms: Fourier transform, Kirchhoff (KKF), and Born–Kirchhoff (BK)

interpolators for mild, moderate, and large to strong lateral heterogeneities, respectively. The validity of these interpolators has been validated by the 2D SEG/EAGE salt model and practical applications to field data (Fu *et al.* 2013).

The motivation of this work is to extend the 2D KKF and BK interpolators to 3D cases for 3D large-step Fourier migrations to reduce computational costs while preserving Fourier imaging accuracy. As described in Appendix A, we first extend the 2D SVSP1 Fourier extrapolator (Fu 2006) to 3D cases for large-step wavefield extrapolation. The 3D KKF interpolator is then derived from the traditional 3D KKF integral formula and used to interpolate wavefields for moderate lateral velocity variations. The 3D BK interpolator is formulated based on the 3D Lippmann–Schwinger integral equation under the Born approximation over a perturbation slab. This strategy is suited for salt-related complex structures that are commonly associated with large to strong lateral velocity variations. The 3D BK interpolator presents a simple algorithm structure with complexity and computational cost nearly equal to those of the KKF interpolator. We discuss the practical aspects of 3D Fourier wavefield extrapolation, focusing on the efficiency of wavefield extrapolation by optimising migration parameters. Numerical results from the cascaded application of the SVSP1 method and the 3D KKF or BK interpolator to the 3D SEG/EAGE salt model illustrate the feasibility of our strategy. Fourier depth migrations by a 72-ms depth size with the BK interpolator lead to a nearly 80% reduction of computational time in contrast to the desired migration using the grid interval of 10 m without interpolation. These interpolation techniques result in considerable savings of computing time and memory for 3D Fourier migrations. Although the proposed 3D interpolators are presented with one-way Fourier extrapolators, they can be extended for applications to a general migration method.

THREE-DIMENSIONAL WAVEFIELD INTERPOLATION INSIDE A SLAB

The standard Kirchhoff migration formula (French 1975; Schneider 1978) can be reduced to an efficient wavefield interpolation algorithm to interpolate wavefields in large-step Fourier migrations. Bevc (1997) extended this time–space Kirchhoff migration into the frequency–space domain, and based on the result, Fu (2004) proposed the 2D KKF interpolator formulated from the Kirchhoff migration formula in the frequency–space domain (Bevc 1997). We extend this understanding to the 3D wavefield interpolator, where each downward-continued wavefield at $(x_p, y_p, z + \Delta z_{\min})$ is

calculated by integration over the input wavefields around (x_p, y_p, z) as

$$u(x_p, y_p, z + \Delta z_{\min}) = \iint \frac{\sqrt{-ik_0}\cos(\theta)}{2\pi r(x, y)\sqrt{v_0}}$$
$$\times u(x, y, z)\exp(ik_0 r(x, y))dxdy, \qquad (1)$$

where $r(x, y) = \sqrt{(x_p - x)^2 + (y_p - y)^2 + \Delta z_{\min}^2}$; v_0 and k_0 are the background velocity and the reference wavenumber of a slab, respectively; and θ is the angle between the travel path $r(x, y)$ and the normal to the input interface at depth z. Denoting the continuous coordinates x and y with input trace indexes i and j, respectively, and replacing $\cos(\theta)$ with $\Delta z_{\min}/r_{ij}$, equation (1) can be discretised as

$$u(x_p, y_p, z + \Delta z_{\min}) = \sum_{i=-L_x/2}^{L_x/2} \sum_{j=-L_y/2}^{L_y/2} W_{ij} u_{ij}(z), \qquad (2)$$

where $L_x \times L_y$ is the integral aperture and W_{ij} is the weighting factor

$$W_{ij} = \frac{\Delta z_{\min}\sqrt{-ik_0}\exp(ik_0 r_{ij})}{2\pi r_{ij}^2 \sqrt{v_0}}, \qquad (3)$$

which can be optimally designed using the theory of migration aperture (Schleicher *et al.* 1997). Equation (2) describes the discretised 3D KKF interpolator that can be used to calculate local wavefields for small layers inside each thick slab. Current industry techniques have widely used the 2D/3D KKF interpolator for wavefield interpolation in recursive seismic migrations. However, it is only valid for moderate lateral heterogeneities. In this article, we use it as the reference for the proposed 3D BK interpolator.

The extension of the 3D KKF interpolator to large to strong lateral heterogeneities invokes the 3D BK interpolator. For simplicity, we begin with the 3D Lippmann–Schwinger integral equation in the frequency–space domain

$$u(\mathbf{r}) = u_0(\mathbf{r}) + k_0^2 \iiint O(\mathbf{r}')u(\mathbf{r}')G(\mathbf{r}, \mathbf{r}')d\mathbf{r}', \qquad (4)$$

where $u_0(\mathbf{r})$ is the reference wavefield satisfying the homogeneous Helmholtz equation with the solution being the Kirchhoff propagator defined by equation (1); $O(\mathbf{r}') \approx n(\mathbf{r}') - 1$ is the relative slowness perturbation with $n(\mathbf{r})$ being the refractive index; and $G(\mathbf{r}, \mathbf{r}') = \frac{i}{8\pi^2}\int_{-\infty}^{\infty}\int_{-\infty}^{\infty} k_z^{-1}\exp[ik_z(z - z') + ik_y(y - y') + ik_x(x - x')]dk_x dk_y$ is the 3D causal Green's function satisfying the homogeneous Helmholtz equation. This equation is the extension of the 3D KKF integral equation to lateral heterogeneities, which propagates a time-harmonic wavefield $u(\mathbf{r}')$ through a perturbation slab spanning from z to $z + \Delta z_{\min}$.

Equation (4) describes two-way wave propagation because the full-wavefield Green's function handles both primaries and multiples inside the perturbation slab by solving a system of equations. Calculating $u(\mathbf{r})$ may be impractical due to the volume integration of the unknown wavefield $u(\mathbf{r}')$. Nevertheless, the problem can be properly resolved by reducing the equation to a one-way wavefield extrapolator with the help of the Born approximation, i.e., by replacing the unknown field $u(\mathbf{r}')$ at depth $z + \Delta z$ with the input field $u(\mathbf{r}')_z$ at depth z in equation (4) to yield

$$u(\mathbf{r}) = u_0(\mathbf{r}) + k_0^2 \iiint O(\mathbf{r}')u(\mathbf{r}')_z G(\mathbf{r}, \mathbf{r}')d\mathbf{r}'. \qquad (5)$$

Each downward-continued output trace at $(x_p, y_p, z + \Delta z_{\min})$ is calculated by equation (5) with integration over the input traces

$$u(x_p, y_p, z + \Delta z_{\min})$$
$$= u_0(x_p, y_p, z + \Delta z_{\min}) + \frac{k_0^2 \Delta z_{\min}}{4\pi r(x, y)}\iint O(x, y)u(x, y, z)$$
$$\times \exp(ik_0 r(x, y))dxdy. \qquad (6)$$

Considering $u_0(x_p, y_p, z + \Delta z_{\min})$ as expressed by equation (1), we obtain

$$u(x_p, y_p, z + \Delta z_{\min}) = \iint W(x, O(x, y), k_0)u(x, y, z)dxdy, \qquad (7)$$

where $W(x, O(x, y), k_0)$ represents the weighting coefficient

$$W(x, O(x, y), k_0)$$
$$= \frac{\left(\sqrt{-ik_0/v_0}\cos(\theta) + 0.5 O(x, y)k_0^2 \Delta z_{\min}\right)\exp(ik_0 r(x, y))}{2\pi r(x, y)}. \qquad (8)$$

The weighting coefficient in equation (8) differs from that of the Kirchhoff in equation (3) in not only the obliquity, spherical spreading, and wavelet shaping factors but also the relative slowness perturbation $O(x, y)$ accounting for lateral velocity variations. Because of the application of the Born approximation, Fu (2004) called equation (7) the BK interpolator to differentiate it from the KKF interpolator in its ability to accurately deal with large lateral heterogeneous media. Similar to the KKF interpolator, equation (7) can be discretised within a finite aperture of $L_x \times L_y$ as

$$u(x_p, y_p, z + \Delta z_{\min}) = \sum_{i=-L_x/2}^{L_x/2} \sum_{j=-L_y/2}^{L_y/2} W_{ij} u_{ij}(z). \qquad (9)$$
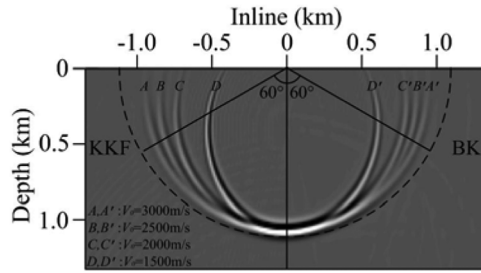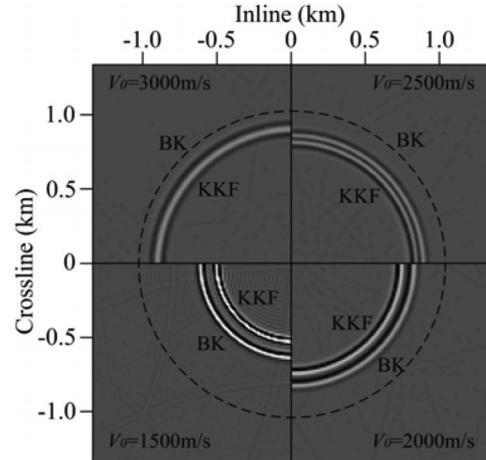
Figure 1 Vertical slices of the 3D impulse responses obtained by the KKF (the left side of the panel) and BK (the right side of the panel) migrators using different reference velocities. The grid interval used here is 10 m, and the dominant frequency of the Ricker wavelet is 30 Hz.

Appendix C presents the accuracy analysis of the BK interpolator using the dispersion equation (named the extended Born dispersion relation) derived from the one-way Lippmann–Schwinger wave equation (B12). As shown in Fig. C1, the BK interpolator presents higher accuracy than the SSF propagator. Appendix C also provides an *f-k* domain version of the BK interpolator despite its instability because of the singularity at large-angle propagation.

Figure 1 shows the vertical slices of the 3D migration impulse responses obtained by both the KKF (the left side of the panel) and BK (the right side of the panel) migrators. The real velocity of the homogeneous media is $V = 4000$ m/s, which leads to a standard semicircle in the panel indicated by the dashed line. The reference velocities for *A* and *A'*, *B* and *B'*, *C* and *C'*, and *D* and *D'* are 3000, 2500, 2000, and 1500 m/s respectively (i.e., velocity contrasts calculated by $(V - V_0)/V$ are 25%, 37.5%, 50%, and 62.5%, respectively). Each BK response clearly deviates from the exact position less than the KKF under the same velocity contrast, which presents better adaptability to the velocity variation of the BK method.

Figure 2 displays the depth slices of 3D migration impulse responses at the depth where the radius of the right circle poses a dip angle of 60° relative to the depth direction. This figure yields a more explicit comparison of the two methods. The entire panel is divided into four equipment parts, and each part shows the responses of both the BK and KKF methods, as well as the correct position (marked with the dashed line) under different reference velocities. The upper left quadrant represents $V_0 = 3000$ m/s, the upper right quadrant represents $V_0 = 2500$ m/s, the lower left quadrant represents $V_0 = 2000$ m/s, and the lower right quadrant represents $V_0 = 1500$ m/s. As shown in the figure, the two responses overlap onto each other and slightly deviate from the dashed line when the velocity contrast is lower than 37.5% (i.e., $(V - V_0)/V \le$

Figure 2 Depth slices of 3D impulse responses obtained by the KKF and BK migrators using different reference velocities. The grid interval used here is 10 m, and the dominant frequency of the Ricker wavelet is 30 Hz.

37.5%, the upper half part of the panel). Hence, the two methods are similarly efficient if a relatively small velocity contrast is involved. As the divergences of the real velocity and reference velocity increase (the lower half part of the panel), both responses migrate away from the ideal position, but the BK method shows a lower migration speed than the KKF one. The gradually increasing gap between the two responses reveals the superior performance of the BK method in dealing with high-velocity contrast.

OPTIMAL IMPLEMENTATION OF EXTRAPOLATION AND INTERPOLATION

Current industry techniques of Fourier migrations usually require 32- to 40-ms depth intervals for wavefield extrapolation, followed by wavefield interpolation using the KKF interpolator for small layers at Δz_{min} spacing inside each thick slab. In Fourier depth migration, frequency-related parameters and depth-step sizes are the key factors affecting computational efficiency and imaging accuracy. This section presents some original techniques to optimise these parameters for Fourier wavefield extrapolation.

The migration sampling rate Δt_{mig}, frequency increment $\Delta\omega$, and number of frequencies to migrate n_ω are the dominant frequency parameters contributing to the performance of Fourier migration. Usually, Δt_{mig}, which is defined as $\Delta t_{mig} = 0.5/f_{max}$, with f_{max} as the maximum frequency to migrate, is much larger than the sampling rate Δt of the input seismic data. We use Δt_{mig} to calculate the frequency
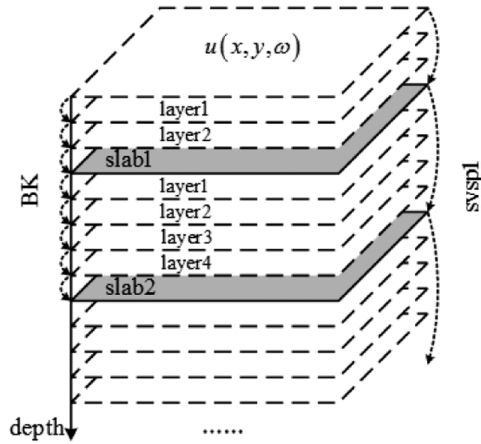
Figure 3 Large-step wavefield extrapolation is conducted through a thick slab by the SVSP1 propagator. The migrated wavefields for small heterogeneous layers defined by Δz_{min} are then interpolated inside the thick slab by the BK operator.

increment $\Delta \omega$, i.e., $\Delta \omega = 2\pi/(L\Delta t_{mig})$, rather than the general expression $\Delta \omega = 2\pi/(N_t \Delta t)$, with L representing N_t the original time sampling points and the two-radix FFT length, respectively. The minimum layer thickness Δz_{min} required for seismic migration is also determined by Δt_{mig}. As a consequence, the number of frequencies n_ω is reduced to save computing time. Prior to migration, the input seismic data are Fourier translated into the frequency–space domain according to N_t and Δt, and the resulting complex wavefield is interpolated in terms of the new frequency increment $\Delta \omega$ to generate the wavefield for extrapolation.

Depth-step size is another crucial parameter that must be properly selected for wavefield extrapolation. The depth-step size as an input parameter is in units of milliseconds, which can be mapped during depth migration into a depth interval in metres in terms of velocities in each slab. That is, Fourier wavefield extrapolation during depth migration will be performed using a large depth size for large-velocity slabs or a small depth size for small-velocity slabs. This process can be easily achieved by designing a time parameter in milliseconds, but this parameter should be appropriately estimated by analysing the heterogeneity and angular spectra of the velocity (Fu 2010; Dong *et al.* 2011; Fu *et al.* 2013) because no efficient criterion has yet been found to evaluate variable depth intervals for laterally heterogeneous slabs. In general, the more accurate the migrator is, the larger the depth range it can tolerate. However, excessively large depth-step sizes will cause discontinuities along dipping reflectors at discrete intervals related to depth-step size (Yilmaz 1987). In principle, these

spurious kinks could be removed by local wavefield interpolation. More precise interpolation algorithms (e.g., the BK interpolator) are required for stronger lateral heterogeneities. Based on 2D numerical tests (Fu 2004) on the SEG/EAGE salt model, larger depth intervals (e.g., 40–60 ms) can be used for wavefield extrapolation when accompanied by the BK interpolator for depths at Δz_{min} spacing inside each interval. In 3D cases, the procedure of wavefield extrapolation through thick slabs and wavefield interpolation at small layers defined by Δz_{min} inside each thick slab is shown in Fig. 3.

NUMERICAL EXAMPLES

Figure 4 provides vertical slices of the 3D impulse responses obtained by the large-step wavefield extrapolator (SVSP1) plus the small-step wavefield interpolators (i.e., (a) KKF and (b) BK). The real velocity of the homogeneous medium and the reference velocity used here are $V = 4000$ m/s and $V_0 = 2500$ m/s, respectively. The grid interval for both vertical and horizontal directions is 10 m, and the dominant frequency of the Ricker wavelet is 30 Hz. On the one hand, the outlines of both responses in (a) and (b) match the ideal position of the reflection indicated by the black dashed line well, even at an angle of 70°; the response shows no noticeable deviation from the exact position. This result demonstrates the excellent accuracy of the SVSP1 migrator. On the other hand, the comparison between the two responses presents the advantages of the BK interpolator because the results in Fig. 4(a) are more continuous than those revealed in Fig. 4(b). In the following section, more detailed numerical examples are provided for the comparison of the two interpolators.

To verify the efficiency and accuracy of the 3D SVSP1 plus KKF and BK interpolator methods, we tested them on the zero-offset records of the 3D SEG/EAGE salt model. The velocity model used here has $500 \times 500 \times 401$ grid points, 20-m spacings in the x- and y-directions, and a 10-m spacing in the z-direction. It is generated from the 3D SEG/EAGE salt model that has $250 \times 250 \times 201$ grid points with 40-m spacings in the x- and y-directions and a spacing of 20 m in the z-direction using two-point linear interpolation. The 3D zero-offset records are also interpolated using the same linear interpolation to match the model. The frequency range calculated in the extrapolation is 0–30 Hz. All post-stack migrations are computed on an Intel® Xeon® E5620 processor (1600 MHz) with a random access memory device of 4 Gb on a 64-bit Linux platform. Figure 5(a) and (c) displaces a horizontal slice at a depth of 2100 m and a vertical slice along the inline direction at a crossline position of 5000 m, respectively.
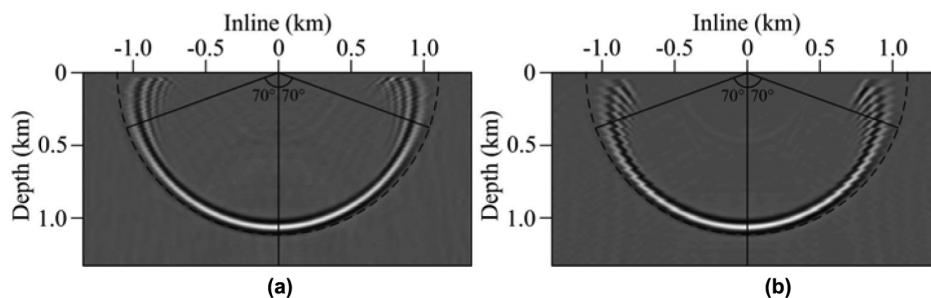
Figure 4 Vertical slices of 3D impulse responses obtained by (a) the SVSP1 + BK method and (b) the SVSP1 + KKF method. The velocity of the homogeneous medium here is $V = 4000$ m/s, and the reference velocity is $V_0 = 2500$ m/s. The dashed semicircle represents the ideal position. The grid interval used here is 10 m, and the dominant frequency of the Ricker wavelet is 30 Hz.
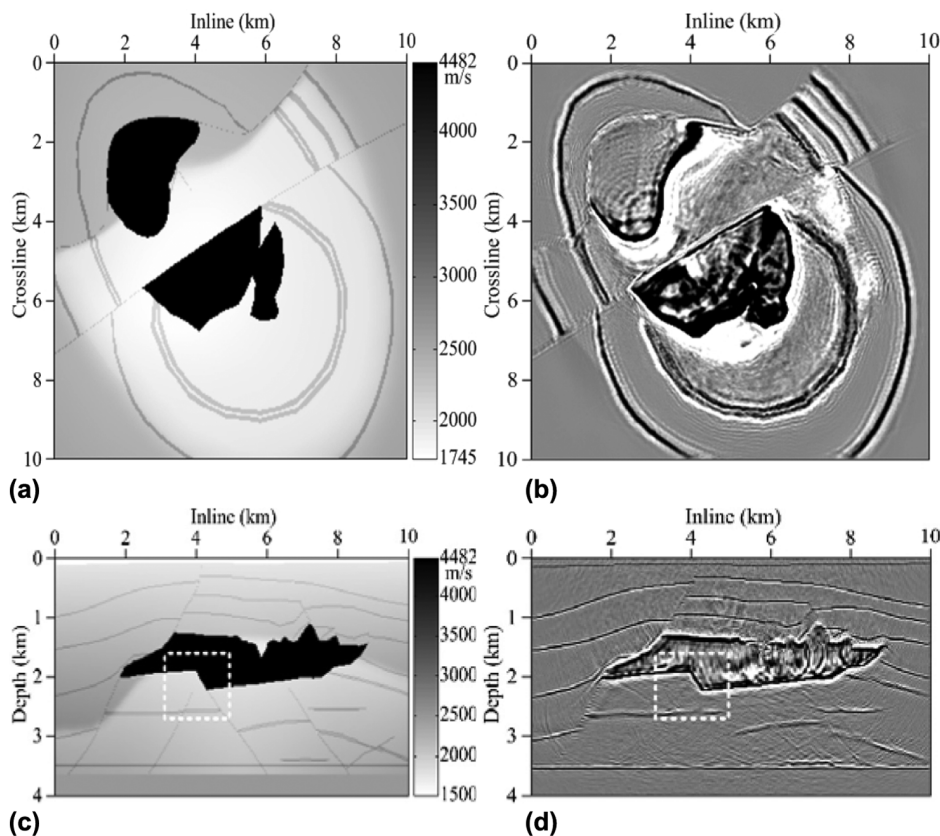
Figure 5 (a) A horizontal slice of the model at a 2100-m depth and (b) its desired migration using the minimum 10-m depth step without wavefield interpolation. (c) A vertical inline slice at crossline 5000 m and (d) the desired migration section.

Figure 5(b) and (d) show the corresponding desired migration sections using the pure SVSP1 method with the minimum 10-m depth step (the grid spacing of the velocity model) without wavefield interpolation.

Although the SVSP1 extrapolator is able to tolerate relatively large depth steps for highly laterally heterogeneous media, it requires appropriate selection to avoid severe spurious kinks along steep dips. Based on experience, we chose

the time parameters of 32 and 72 ms for downward wavefield extrapolation. In this work, depth-step sizes are measured in milliseconds rather than metres to enable the migration program to calculate real-time depth steps according to velocity variations. For example, a 72-ms depth step allows extrapolation slabs to vary in thickness from 108 to 324 m corresponding to a range of velocity changes from 1500 to 4500 m/s.
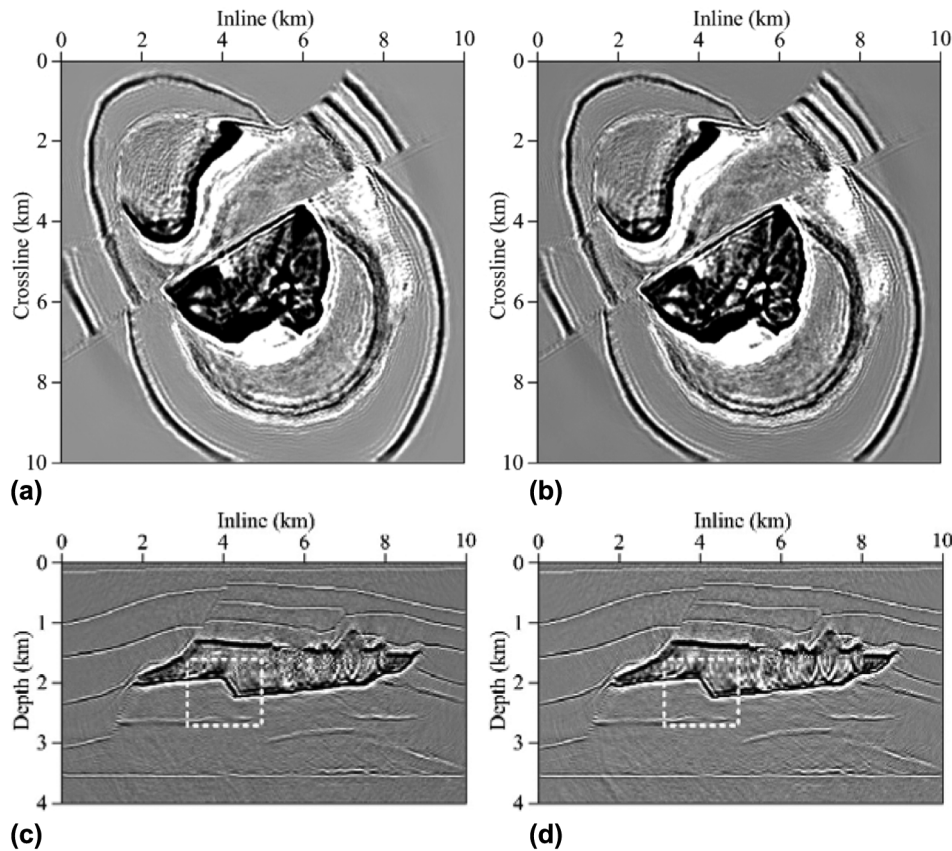
Figure 6 Horizontal and vertical migration slices resulting from (a, c) the 32-ms SVSP1-KKF method and (b, d) the 32-ms SVSP1-BK method.

Figure 6(a) and (c) illustrates the horizontal and vertical sections migrated by the 32-ms SVSP1 + KKF method, whereas Fig. 6(b) and (d) illustrates the corresponding sections migrated by the 32-ms SVSP1 + BK method. Compared with the desired migration in Fig. 5(b) and (d), both the KKF and BK interpolators show nearly no reduction of imaging quality, except for the negligible distortion within the salt body. Considering the absence of significant differences between the migration sections, distinguishing these two interpolators in terms of imaging accuracy is difficult when depending solely on Fig. 6, mainly because depth steps calculated using the 32-ms parameter are only two to four times as large as the grid spacing.

Increasing the depth-step size to 72 ms leads to the migration results shown in Fig. 7. Because of phase errors caused by the KKF interpolator, Fig. 7(a) shows poorer spatial resolution than Fig. 5(b) because of stretching of the structure interfaces and the appearance of noticeable spurious kinks accompanied with a slight smearing of waveforms along the steep dips in Fig. 7(c). In Fig. 7(b) and (d), the more accurate BK interpolator does not apparently deteriorate the imaging quality in

comparison with the desired migration. The absence of visible kinks further indicates that the 72-ms BK interpolator is not too coarse for the dips presented in the model. Although 72 ms is an excessively large depth step, it can still produce adequate results for the salt model with strong-contrast heterogeneities and steep dips. Thus, Fig. 7 confirms that the BK interpolator outperforms the KKF interpolator when large depth-step sizes are involved.

Figure 8 provides a clearer comparison of the two migration strategies by enlarging the rectangular areas in Figs. 5, 6, and 7. Figure 8(c) and (d) shows results comparable with the desired migration in Fig. 8(b) in terms of the sloping edge of the salt body (indicated by black arrows). This result demonstrates that the SVSP1 + KKF and SVSP1 + BK methods are fairly suitable for the model when a relatively short time parameter, such as 32 ms, is selected. The 72-ms results of the SVSP1 + KKF and SVSP1 + BK methods are shown in Fig. 8(e) and (f), respectively. The obvious discontinuity within the salt body and the zigzags along the steep salt edge in Fig. 8(e) shows that the 72-ms time parameter is slightly large for the SVSP1 + KKF method. By comparison, the SVSP1 + BK
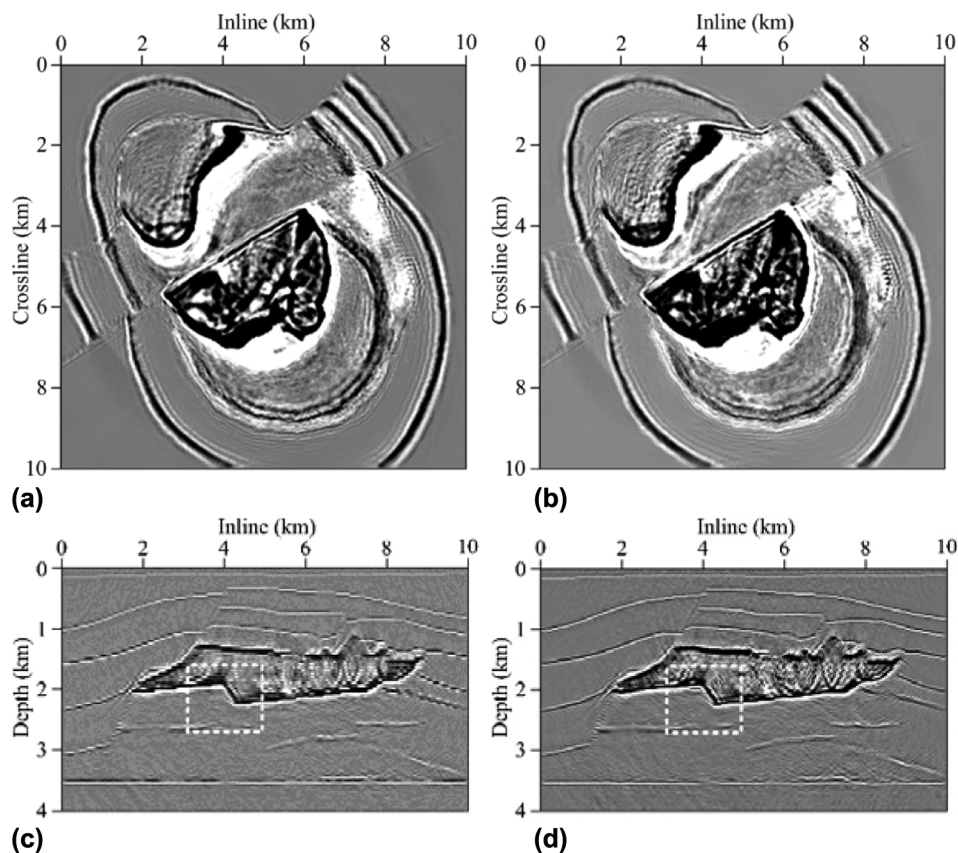
Figure 7 Horizontal and vertical migration slices resulting from (a, c) the 72-ms SVSP1 + KKF method and (b, d) the 72-ms SVSP1 + BK method.

method using the 72-m parameter yields acceptable results, and no measurable distortion can be seen in Fig. 8(f) despite the weak discontinuity within the salt body. Thus, the BK interpolator achieves better migration than the KKF interpolator, especially when a relatively large time parameter is used.

Figure 9 plots the depth-step variation along the depth direction using 32 and 72 ms as depth parameters; in the figure, the dashed line represents the 32-ms case, which has a total step number of 108, and the solid line represents the 72-ms case, which shows larger depth step changes and has a step number of only 54. As the depth increases, the step sizes of both cases also increase, mainly because the total velocity shows a generally increasing trend in the depth direction. We note here that, although the two curves show similar shapes, they are not quantitatively related to each other because of the randomness of the velocity distribution. Bumps peaking at a depth of about 1800 m are caused by the relatively high reference velocity attributed to the high velocity of the salt body.

Table 1 compares the CPU time of these post-stack migrations on the 3D SEG/EAGE salt model with different

Table 1 CPU time of post-stack migrations with different depth-step sizes for the 3D SEG/EAGE salt model

Method	Depth step	CPU time
SVSP1	10 m	3376 s
SVSP1 + Kirchhoff	32 ms	1052 s
SVSP1 + Born–Kirchhoff	32 ms	1065 s
SVSP1 + Kirchhoff	72 ms	809 s
SVSP1 + Born–Kirchhoff	72 ms	820 s

depth-step sizes. Nearly equal computational times are required for both the SVSP1 + KKF and the SVSP1 + BK methods to migrate the zero-offset records as the same time parameters are used. Compared with the pure SVSP1 migration, both methods for the 32-ms case reduce the CPU time by about 68%, and this time reduction increases to about 79% when the 72-ms parameter is used. We tested other time parameters larger than 72 ms but obtained limited time savings, largely because more wavefield interpolations, which demand more computing time, are required for large depth steps.
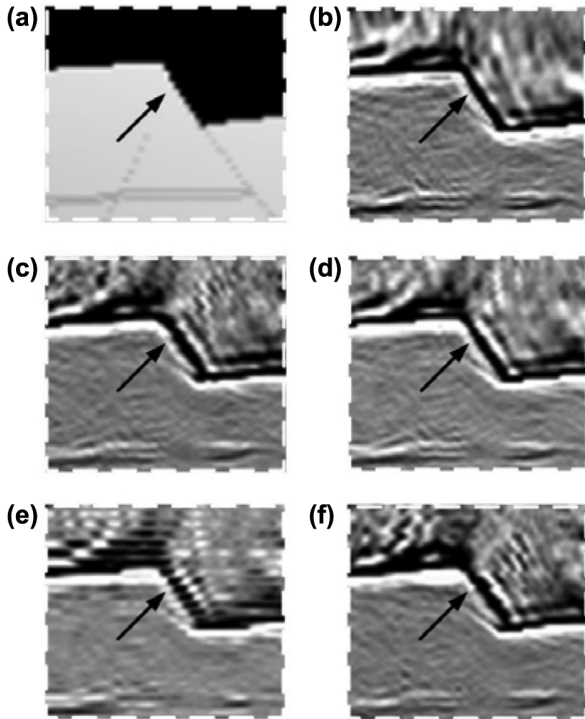
Figure 8 Comparison of the local details within the rectangular areas in Figs. 5, 6, and 7: (a) The velocity model; (b) the desired migration; (c) 32-ms SVSP1 + KKF migration; (d) 32-ms SVSP1-BK migration; (e) 72-ms SVSP1 + KKF migration; and (f) 72-ms SVSP1 + BK migration.
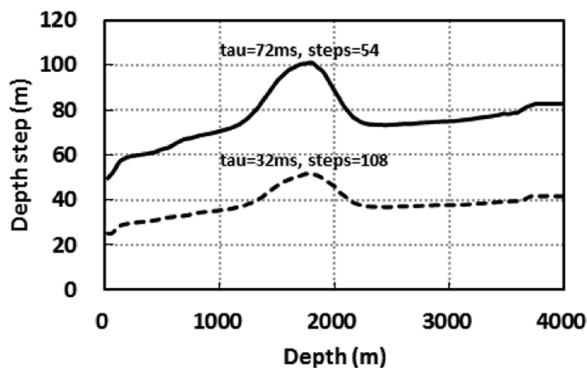

Figure 9 Depth intervals (in metres) of thick slabs versus depth across the whole model for the time input parameters of 32 and 72 ms, corresponding total depth-step numbers of 108 and 54, respectively, for wavefield extrapolation.

SUMMARY AND CONCLUSIONS

Of the many advantages of Fourier-transform-based migrations, the flexibility of depth-step size for wavefield extrapolation is a critical one. In practice, large depth steps are always used to improve efficiency. This strategy, however, produces

spurious kinks along dipping reflectors. These steep-interface distortions can be effectively eliminated by local interpolation within each extrapolation. In this paper, we mainly develop the 3D large-step Fourier wavefield extrapolator and efficient local interpolators for laterally heterogeneous media for the sake of computational efficiency and imaging accuracy.

To guarantee accurate wavefields at large depth-step sizes for laterally varying media, we derive the 3D SVSP1 propagator for large-step extrapolation. The 3D SVSP1 extrapolator uses separation-of-variables decomposition instead of implicit FD implementation to accomplish high-accuracy wavefield correction, which also leads to an efficiency improvement. Migration tests on the 3D SEG/EAGE model using the pure SVSP1 method with minimum grid interval demonstrate its efficiency and effectiveness in dealing with significant lateral velocity variations. To support large-step 3D SVSP1 migration, we develop the 3D KKF and BK interpolators to dispose of the spurious kinks observed during moderate and strong lateral velocity variations, respectively. These two interpolators are in fact local wavefield extrapolators and can correct distorted wavefields by taking into account spherical spreading, wavelet shaping, and relative slowness perturbations. Prior to each wavefield extrapolation, a time parameter is applied to determine the depth of the current step according to the velocity distribution.

Numerical tests on the 3D SEG/EAGE model show the success of both SVSP1 + KKF and SVSP1 + BK methods in accuracy and efficiency when a relatively small time parameter is used. Appropriately increasing the time parameter results in significant time savings despite the negligible imaging deterioration. We acknowledge that increases in the time parameter result in smaller and smaller time reductions because of the growing number of interpolations; the imaging accuracy is also lowered, particularly for the KKF interpolator. Regardless of these observations, the SVSP1 + BK interpolator with a 72-ms depth-step size still achieves high imaging accuracy while saving time consumption by nearly 80% compared with the desired migration using the velocity grid interval of 10 m. Although the proposed 3D interpolators are presented with one-way Fourier extrapolators, they can be extended for applications to general migration methods.

ACKNOWLEDGEMENTS

2013AA064202). The authors would like to extend their grateful thanks to the anonymous reviewers for their professional comments and suggestions.

REFERENCES

Bamberger A., Engquist B., Halpern L. and Joly P. 1988. Higher order paraxial wave equation approximations in heterogeneous media. *SIAM Journal on Applied Mat hematics* **48**(1), 129–154.

Bevc D. 1997. Flooding the topography: Wave-equation datuming of land data with rugged acquisition topography. *Geophysics*, **62**, 1558–1569.

Cheng N., Cheng C.H. and Toksöz M.N. 1996. Error analysis of phase screen method in 3-D. *Geophysical Research Letters* **23**, 1841–1844.

Claerbout J.F. 1985. *Imaging the Earth's Interior*. Blackwell Scientific Publications.

Collins M.D. 1993. A split-step Padé solution for the parabolic equation method. *The Journal of the Acoustical Society of America* **93**, 1736–1742.

Dong W., Fu L.Y., Xiao Y.J., Guan X.Z. and Wu C. 2011. Quantitative analysis of the complexity in seismic exploration of the high and steep. *Chinese Journal of Geophysics* **54**(6), 1600–1613.

De Hoop M., Le Rousseau J. and Wu R.S. 2000. Generalization of the phase-screen approximation for the scattering of acoustic waves. *Wave Motion* **31**, 43–70.

French W.S. 1975. Computer migration of oblique seismic reflection profiles. *Geophysics* **40**, 6–16.

Fu L.Y. 2004. Wavefield interpolation in the Fourier wavefield extrapolation. *Geophysics* **69**(1), 257–264.

Fu L.Y. 2005. Broadband constant-coefficient propagators. *Geophysical Prospecting* **53**, 299–310.

Fu L.Y. 2006. Comparison of different one-way propagators for wave forward propagation in heterogeneous crustal wave guides. *Bulletin of the Seismological Society of America* **96**, 1091–1113.

Fu L.Y. 2010. Quantitative assessment of the complexity of geological structures in terms of seismic propagators. *Science in China Series D: Earth Sciences* **53**, 54–63.

Fu L.Y., Mu Y.G. and Yang H.J. 1997. Forward problem of nonlinear Fredholm integral equation in reference medium via velocity-weighted wavefield function. *Geophysics* **62**, 650–656.

Fu L.Y., Xiao Y.J., Sun W.J., Wu C., Guan X.Z. and Zhang J.Z. 2013. Seismic imaging studies of complex high and steep structure in Kuqa depression. *Chinese Journal of Geophysics* **56**(6), 1985–2001.

Gazdag J. and Sguazzero P. 1984. Migration of seismic data by phase shift plus interpolation. *Geophysics* **49**, 124–131.

Halpern L. and Trefethen L.N. 1988. Wide-angle one-way wave equations. *The Journal of the Acoustical Society of America* **84**, 1397–1404.

Huang L.J. and Fehler M.C. 1998. Accuracy analysis of the split-step Fourier propagator: implications for seismic modeling and migration. *Bulletin of the Seismological Society of America* **88**, 18–29.

Huang L.J., Fehler M.C. and Wu R.S. 1999. Extended local Born Fourier migration method. *Geophysics* **64**, 1524–1534.

Kessinger W. 1992. Extended split-step Fourier migration. 62nd SEG annual international meeting, Expanded Abstracts, 917–920.

Le Rousseau J.H. and De Hoop M.V. 2001. Modeling and imaging with the scalar generalized-screen algorithms in isotropic media. *Geophysics* **66**, 1551–1568.

Liu L. and Zhang J. 2006. 3D wavefield extrapolation with optimum split-step Fourier method. *Geophysics* **71**, T95–T108.

Ristow D. and Rühl T. 1994. Fourier finite-difference migration. *Geophysics* **59**, 1882–1893.

Schleicher J., Hubral P., Tygel M. and Jaya M.S. 1997. Minimum apertures and Fresnel zones in migration and demigration. *Geophysics*, **62**, 183–194.

Schneider W.A. 1978. Integral formulation for migration in two and three dimensions. *Geophysics* **43**, 49–76.

Stoffa P.L., Fakkema J.T., de Luna Freire R.M. and Kessinger W.P. 1990. Split-step Fourier migration. *Geophysics* **55**, 410–421.

Tappert F.D. 1977. The parabolic approximation method. In: *Wave Propagation and Underwater Acoustics*, pp. 224–287. Springer-Verlag.

Thomson D.J. 1990. Wide-angle parabolic equation solutions to two range-dependent benchmark problems. *The Journal of the Acoustical Society of America* **87**, 1514–1520.

Trefethen L.N. and Halpern L. 1986. Well-posedness of one-way equations and absorbing boundary conditions. *Mathematics of Computation* **147**, 421–435.

Wu R.S. 1996. Synthetic seismogram in heterogeneous media by one-return approximation. *Pure and Applied Geophysics* **148**, 155–173.

Wu R.S. and Jin S. 1997. Windowed GSP (generalized screen propagators) migration applied to SEG-EAEG salt model data. 67th SEG annual international meeting, Expanded Abstracts, 1746–1749.

Yilmaz O. 1987. *Seismic Data Processing*. Society of Exploration Geophysicists.

Zhang J.H., Wang W.M., Wang S.Q. and Yao Z.X. 2010. Optimized Chebyshev Fourier migration: a wide-angle dual-domain method for media with strong velocity contrasts. *Geophysics* **75**(2), S23–S34.

APPENDIX A

THREE-DIMENSIONAL LARGE-STEP FOURIER WAVEFIELD EXTRAPOLATION

This appendix extends the 2D SVSP1 Fourier extrapolator (Fu 2006) to 3D cases for large-step wavefield extrapolation. An operator $K(x, y)$ is said to be separation-of-variables if it can be decomposed in the form $K(x, y) = \sum_{k=1}^{N} A_k(x) B_k(y)$, where functions $A_k(x)$ and $B_k(y)$ are linearly independent. In general, higher-order series expansion involves heavy numerical calculations. An efficient development with rapid convergence comes with lower-order terms that satisfy seismic imaging accuracy for large to strong lateral heterogeneities. We will demonstrate that the separation-of-variables expression of the one-way Lippmann–Schwinger integral propagator leads to

a Fourier matching solution for Fourier wavefield extrapolation. These separation-of-variables extrapolators preserve a dual-domain algorithmic structure of the classical phase-screen extrapolator.

As described in Appendix B, the one-way Lippmann–Schwinger integral equation (B12) with complex convolutional operations in $F(k_x, k_y, z)$ accounts for the accumulated effects of both forward scattering inside a heterogeneity slab and transmission/refraction between different slabs on wave amplitude and phase. Appendix C further explores the physics of equation (B12) by the Born approximation, refractive-index smoothing, and small-angle approximation, resulting in several typical low-accuracy dispersion equations; some high-accuracy rational approximations to equation (B12) lead to terms with the cross product of velocity perturbations and propagation angles. The cross terms must invoke a new implicit finite-difference (FD) implementation in Fourier wavefield extrapolation. To avoid this problem, we consider the following separation-of-variables decomposition:

$$\bar{k}_z(\bar{k}_x, \bar{k}_y, n) \approx \sum_{j=1}^{m} f_j(\bar{k}_x, \bar{k}_y) g_j(n). \quad (A1)$$

Thus, we need to handle the following two problems: (i) construction of the splitting operators $f_j(\bar{k}_x, \bar{k}_y)$ and $g_j(n)$ and (ii) pure Fourier transform implementation to equation (A1). We compare the Taylor series expansion and some rational approximations for the construction of these splitting operators. As expected, these two approaches possess quite different properties of approximations.

Using the rectangular rule rather than the trapezoid rule to evaluate the volume integration over the slab in equation (B8) and setting $k_z + k_z' \approx 2k_z$ for convenience, equation (B12) becomes a standard equation for one-way propagation in heterogeneous media

$$u(k_x, k_y, z + \Delta z) = \left[u(k_x, k_y, z) + \frac{1}{k_z} F T_{xy}[i k_0 \Delta z (n(\mathbf{r}) - 1) u(\mathbf{r})] \right] \times \exp(i k_z \Delta z), \quad (A2)$$

where $F T_{xy}$ denotes the 2D Fourier transform from (x, y) to (k_x, k_y). Because of the second term inside the bracket, this equation takes into account the accumulated effect of forward scattering by volume heterogeneities in the slab. The corresponding dispersion relation is shown in equation (C7), which can be rewritten as

$$\bar{k}_z = \sqrt{1 - \bar{k}_x^2 - \bar{k}_y^2} + (n - 1)\left(\sqrt{1 - \bar{k}_x^2 - \bar{k}_y^2} \right)^{-1}. \quad (A3)$$

Equation (A3) is a separation-of-variables operator representation with its accuracy shown in Fig. C1 (marked by EBorn). Equation (A3) is the first-order approximation of Taylor series expansion of the square-root operator. A Fourier-transform-based matching solution to equation (A3) can be obtained from equation (A2) using the approximate calculation $e^{i\zeta} \approx 1 + i\zeta$

$$u(k_x, k_y, z + \Delta z)$$
$$= \left[\left(1 - \frac{1}{\sqrt{1 - \bar{k}_x^2 - \bar{k}_y^2}} \right) + \frac{1}{\sqrt{1 - \bar{k}_x^2 - \bar{k}_y^2}} \exp(i k_0 \Delta z (n - 1)) \right]$$
$$\times u(k_x, k_y, z) \exp(i k_z \Delta z). \quad (A4)$$

The split-step solution to this equation can be expressed as

$$u(k_x, k_y, z + \Delta z)$$
$$= \left[\left(1 - \frac{1}{\sqrt{1 - \bar{k}_x^2 - \bar{k}_y^2}} \right) u(k_x, k_y, z) + \frac{1}{\sqrt{1 - \bar{k}_x^2 - \bar{k}_y^2}} \right.$$
$$\left. \times F T_{xy}[u(x, y, z) \exp(i k_0 \Delta z (n(x, y) - 1))] \right] \exp(i k_z \Delta z). \quad (A5)$$

We see that wavefield extrapolation through a slab by the first-order separation-of-variables propagator is a linear interpolation in the wavenumber domain between the reference phase-shift solution and the split-step solution. The computational time with equation (A5) is almost the same as the traditional SSF solution.

The problems with the Taylor degenerate operator approximation (A5) are as follows: (i) low accuracy (although better than the SSF method) that causes poor performance for strong-contrast slabs and (ii) singularity when $\bar{k}_x^2 + \bar{k}_y^2 \approx 1$ (high propagation angles). This singularity is the main reason for unstable numerical propagation for large lateral variations, high frequencies, and large propagation angles. Replacing $\sqrt{1 - \bar{k}_x^2 - \bar{k}_y^2}$ in equation (A5) with $\sqrt{1 - \bar{k}_x^2 - \bar{k}_y^2} + \sqrt{1 - \bar{k}_x'^2 - \bar{k}_y'^2}$ (see equation (C4)) may reduce the singularity to some degree due to the velocity difference between adjacent slabs.

The phase error brought about by the parabolic correction term in equation (C10) rapidly increases with increasing $\bar{k}_x^2 + \bar{k}_y^2$ and decreasing n. In such circumstances, approximation to the parabolic correction term will yield more accurate
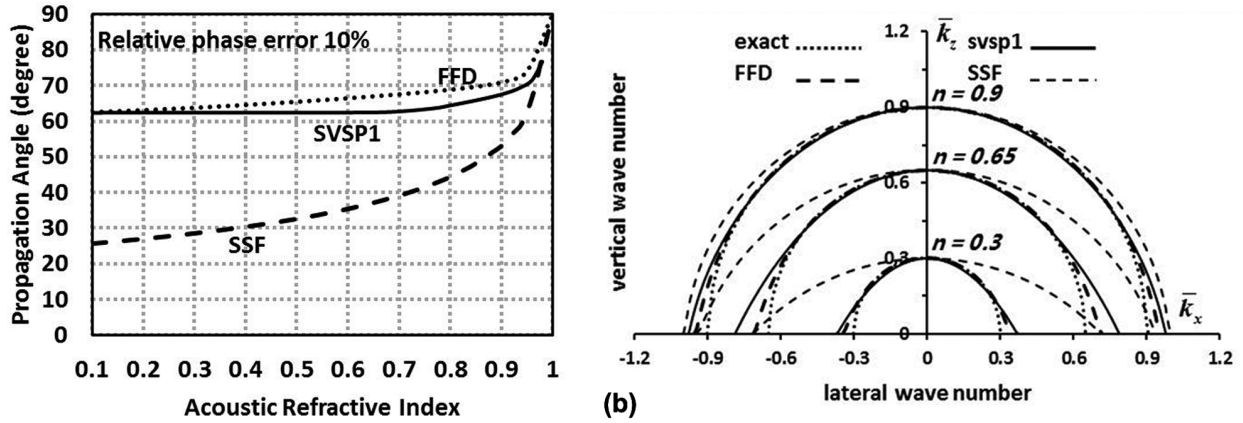
Figure A1 Accuracy analysis of the first-order SVSP1. (a) Angular spectra of (solid line) the SVSP1 propagator compared with those of (dotted line) the FFD and (dashed line) the SSF propagators. (b) Dispersion circles of (thick solid line) the SVSP1 propagator compared with those of (thick dotted line) the exact, (thick dashed line) the FFD, and (thin dashed line) the SSF propagators for $n = 0.3$, $n = 0.65$, and $n = 0.9$.

results if some fast convergent functions, such as rational, exponential, or logarithmic functions, are applied, rather than the Taylor series expansion, for a given number of terms. In analogy to the FD-based various parabolic approximations to the square-root operator, more accurate operator approximations for constructing the splitting operators in equation (A1) can be obtained with the use of rational functions.

Since $\bar{k}_x^2 + \bar{k}_y^2 \leq 1$ for one-way propagation, the term $(1 - \bar{k}_x^2 - \bar{k}_y^2)^{-1/2}$ in equation (A3) can be approximated by the following rational expansion:

$$\left(1 - \bar{k}_x^2 - \bar{k}_y^2\right)^{-1/2} = 1 - \sum_{j=1}^{m} \frac{a_j \left(\bar{k}_x^2 + \bar{k}_y^2\right)}{1 + b_j \left(\bar{k}_x^2 - \bar{k}_y^2\right)}, \qquad (A6)$$

where coefficients a_j and b_j are independent from n. Substituting this equation into equation (A3), we obtain

$$\bar{k}_z = \sqrt{1 - \bar{k}_x^2 - \bar{k}_y^2} + n - 1 - (n-1) \sum_{j=1}^{m} \frac{a_j \left(\bar{k}_x^2 + \bar{k}_y^2\right)}{1 + b_j \left(\bar{k}_x^2 + \bar{k}_y^2\right)}. \qquad (A7)$$

In comparison with the Fourier finite-difference (FFD) solution (C10), equation (A7) is a separation-of-variables operator representation that leads to a pure Fourier-transform-based matching solution.

Coefficients in equation (A7) can be determined numerically by an optimization procedure using least-squares method. The optimization procedure can be defined as searching optimal a_j and b_j to minimize the following cost function

$$J = \int_0^1 \int_0^{\phi} E^2(\theta, n) d\theta dn, \qquad (A8)$$

where ϕ is the maximum angle designed and the dispersion error

$$E(\theta, n) = \sqrt{1 - \bar{k}_x^2 - \bar{k}_y^2} + n - 1 - (n-1) \sum_{j=1}^{m} \frac{a_j \left(\bar{k}_x^2 + \bar{k}_y^2\right)}{1 + b_j \left(\bar{k}_x^2 + \bar{k}_y^2\right)}$$

$$- \sqrt{n^2 - \bar{k}_x^2 - \bar{k}_y^2}. \qquad (A9)$$

Because of the mathematical properties and approximation behaviour of rational functions (e.g., Trefethen and Halpern 1986; Bamberger *et al.* 1988; Halpern and Trefethen 1988), equation (A7) should be well-posed, especially for lower-order terms. In practice, the first-order equation or, at most, the second-order equation is adequate for common one-way propagation in large to strong-contrast media with large propagation angles in seismology.

In the following section, we formulate these separation-of-variables propagators by a Fourier-transform-based representation for numerical implementation. Substituting equation (A7) into (A2) and, using the approximate calculation $e^{i\zeta} \approx 1 + i\zeta$, we obtain

$$u(k_x, k_y, z + \Delta z)$$

$$= \left[\sum_{j=1}^{m} \frac{a_j \left(\bar{k}_x^2 + \bar{k}_y^2\right)}{1 + b_j \left(\bar{k}_x^2 + \bar{k}_y^2\right)} + \left(1 - \sum_{j=1}^{m} \frac{a_j \left(\bar{k}_x^2 + \bar{k}_y^2\right)}{1 + b_j \left(\bar{k}_x^2 + \bar{k}_y^2\right)}\right) \right.$$

$$\left. \times \exp(ik_0 \Delta z(n-1)) \right] u(k_x, k_y, z) \exp(ik_z \Delta z). \qquad (A10)$$

We see that advancing wavefields through a slab results from a linear interpolation in the *f-k* domain between the reference phase-shift solution and the split-step solution. Setting $C_j = a_j(\bar{k}_x^2 + \bar{k}_y^2)/(1 + b_j(\bar{k}_x^2 + \bar{k}_y^2))$ and taking its first-order term (SVSP1), the split-step Fourier (SSF) solution to equation (A10) can be expressed as

$$u(k_x, k_y, z + \Delta z) = \{C_1 u(k_x, k_y, z) + (1 - C_1)FT_{xy}[u(k_x, k_y, z)$$
$$\times \exp(ik_0\Delta z(n-1))]\}\exp[ik_z\Delta z]. \quad (A11)$$

With the first-order separation-of-variables screen propagator (SVSP1), the extrapolated wavefields result from a linear interpolation in the *f-k* domain between two split-step terms $\exp[ik_0\Delta z(n-1)]$ and $\exp[ik_0\Delta z2(n-1)]$. This is the most distinct feature that differentiates the present strategy from the Taylor series expansion. It extends the SSF method to steeper-propagation angles in larger-contrast media at the cost of one more Fourier transform for each extrapolation step. Figure A1 shows the SVSP1's angular spectrum under a relative phase error of 10% in comparison with those of the SSF and FFD propagators. SVSP1 can clearly be regarded as an efficient alternative to the FFD method (Ristow and Rühl 1994) in terms of accuracy but only uses Fourier transforms for migration, thereby significantly reducing computational costs, particularly for 3D cases.

APPENDIX B

ONE-WAY THREE-DIMENSIONAL LIPPMANN–SCHWINGER INTEGRAL PROPAGATOR

In general, most acoustic media in seismic exploration can be sliced into heterogeneous slabs roughly perpendicular to the main propagation direction. Wave propagation in a heterogeneous slab can be formulated as the superposition of incident, boundary scattering, and volume-scattering waves, which can be accurately expressed as the generalised Lippmann–Schwinger integral equation incorporating boundary scattering. This appendix illustrates a brief derivation of the one-way 3D Lippmann–Schwinger integral propagator by one-way approximations from the generalised Lippmann–Schwinger integral equation inside a 3D heterogeneous slab.

Figure B1 depicts the geometry of such a heterogeneous slab with the thickness Δz, denoted by Ω with a top interface Γ_0, a bottom interface Γ_1, and two infinite boundaries Γ_∞. The velocity distribution in the slab is denoted by $v(\mathbf{r})$, where $\mathbf{r}$ is the position vector, and its reference velocity is v_0. We
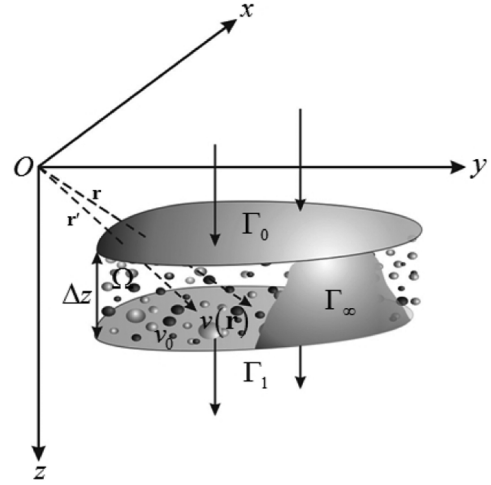

Figure B1 The geometry of a 3D heterogeneous slab.

start with the scalar Helmholtz equation for a time-harmonic wavefield $u(\mathbf{r})$

$$\nabla^2 u(\mathbf{r}) + k^2 u(\mathbf{r}) = 0, \quad (B1)$$

where the wavenumber $k = \omega/v(\mathbf{r})$. The total wavefield Ω at location Ω is composed for scattering problems of

$$u(\mathbf{r}) = u_1^s(\mathbf{r}) + u_2^s(\mathbf{r}). \quad (B2)$$

Ω is the scattered field by the boundary structure $\Gamma = \Gamma_0 + \Gamma_1 + \Gamma_\infty$ and satisfies the following boundary integral equation:

$$u_1^s(\mathbf{r}) = \int_\Gamma \left[G(\mathbf{r}, \mathbf{r}')\frac{\partial u(\mathbf{r}')}{\partial n} - u(\mathbf{r}')\frac{\partial G(\mathbf{r}, \mathbf{r}')}{\partial n} \right] d\mathbf{r}', \quad (B3)$$

where Ω denotes differentiation with respect to the outward normal of the boundary Ω. Ω is the scattered field by the volume heterogeneities within the slab and satisfies the following Lippmann–Schwinger integral equation:

$$u_2^s(\mathbf{r}) = k_0^2 \int_\Omega O(\mathbf{r}')u(\mathbf{r}')G(\mathbf{r}, \mathbf{r}')d\mathbf{r}', \quad (B4)$$

where k_0 is the reference wavenumber and $O(\mathbf{r})$ is the relative slowness perturbation defined as $O(\mathbf{r}) = n^2(\mathbf{r}) - 1$ with the acoustic refractive index $n(\mathbf{r}) = v_0/v(\mathbf{r})$. We define the following velocity-weighted wavefield $F(\mathbf{r}) = ik_0\Delta zO(\mathbf{r})u(\mathbf{r})$ that has a concise relation to scattered fields in the frequency–wavenumber domain (Fu, Mu and Yang 1997).

These Helmholtz integral representation formulas are derived using the Green's function $G(\mathbf{r}, \mathbf{r}')$ in the background medium, i.e., $G(\mathbf{r}, \mathbf{r}') = \frac{i}{8\pi^2} \int_{-\infty}^{\infty} \int_{-\infty}^{\infty} k_z^{-1} \exp[ik_z(z - z') + ik_y(y - y') + ik_x(x - x')]dk_x dk_y$, for 3D problems with Ω. Substituting equations (A3) and (A4) into equation (A2)

and considering the "boundary naturalisation" of the integral equations, i.e., a limit analysis when the "observation point" $\mathbf{r}'$ approaches the boundary Γ and tends to coincide with the "scattering point" $\mathbf{r}$, we obtain the following generalised Lippmann–Schwinger integral equation:

$$\int_{\Gamma} \left[G(\mathbf{r}, \mathbf{r}') \frac{\partial u(\mathbf{r}')}{\partial n} - u(\mathbf{r}') \frac{\partial G(\mathbf{r}, \mathbf{r}')}{\partial n} \right] d\mathbf{r}'$$

$$+ k_0^2 \int_{\Omega} O(\mathbf{r}') u(\mathbf{r}') G(\mathbf{r}, \mathbf{r}') d\mathbf{r}' = \begin{cases} u(\mathbf{r}) & \mathbf{r} \in \Omega \\ C(\mathbf{r}) u(\mathbf{r}) & \mathbf{r} \in \Gamma, \\ 0 & \mathbf{r} \notin \bar{\Omega} \end{cases} \quad (B5)$$

for all $\mathbf{r}' \in \bar{\Omega} = \Omega + \Gamma$, where coefficient $C(\mathbf{r}) = 1/2$ for a flat Γ. This is a wave integral equation that is equivalent to the Helmholtz equation (B1) and describes two-way wave propagation in the heterogeneous slab.

Equation (B5), as a Fredholm integral equation of the second kind, describes wave propagation in the space–frequency domain. Formulating it in the frequency–wavenumber domain using a plane-wave expansion will lead to quite different numerical schemes. In Fig. B1, we assume wave propagation along the Z-axis, crossing the slab from the slab entrance Γ_0 to the exit Γ_1. Let $q(\mathbf{r}) = \partial u(\mathbf{r})/\partial n$ indicate the acoustic pressure gradient, $\mathbf{r} = (x, y, z)$ represent the observation point, and $\mathbf{r}' = (x', y', z')$ denote the scattering point. Applying the plane-wave representation of the Green's function, $G(\mathbf{r}, \mathbf{r}') = \frac{i}{8\pi^2} \int_{-\infty}^{\infty} \int_{-\infty}^{\infty} k_z^{-1} \exp[ik_z(z - z') + ik_y(y - y') + ik_x(x - x')] \times dk_x dk_y$, to each integrand in equation (B5), we obtain

$$\int_{\Gamma_0} \left[G(\mathbf{r}, \mathbf{r}') q(\mathbf{r}') - u(\mathbf{r}') \frac{\partial G(\mathbf{r}, \mathbf{r}')}{\partial n} \right] d\mathbf{r}'$$

$$= \frac{1}{8\pi^2} \int_{-\infty}^{\infty} \int_{-\infty}^{\infty} \left[\left(ik_z^{-1} q(k_x, k_y, z) + u(k_x, k_y, z) \right) \right.$$

$$\left. \times \exp(ik_z \Delta z) \right] \exp(ik_x x) \exp(ik_y y) dk_x dk_y. \quad (B6)$$

$$\int_{\Gamma_1} \left[G(\mathbf{r}, \mathbf{r}') q(\mathbf{r}') - u(\mathbf{r}') \frac{\partial G(\mathbf{r}, \mathbf{r}')}{\partial n} \right] d\mathbf{r}'$$

$$= \frac{i}{8\pi^2} \int_{-\infty}^{\infty} \int_{-\infty}^{\infty} \left[k_z^{-1} q(k_x, k_y, z + \Delta z) \right] \exp(ik_y y)$$

$$\times \exp(ik_x x) dk_x dk_y. \quad (B7)$$

Using the trapezoid rule to evaluate the volume integration over the slab in equation (B5) yields

$$k_0^2 \int_{\Omega} O(\mathbf{r}') u(\mathbf{r}') G(\mathbf{r}, \mathbf{r}') d\mathbf{r}'$$

$$= \frac{k_0}{4\pi^2} \int_{-\infty}^{\infty} \int_{-\infty}^{\infty} k_z^{-1} \left[F(k_x, k_y, z) \exp(ik_z \Delta z) \right.$$

$$\left. + F(k_x, k_y, z + \Delta z) \right] \exp(ik_y y) \exp(ik_x x) dk_x dk_y. \quad (B8)$$

This is actually a Born approximation applied to the slab. This approximation implies that the heterogeneity of the slab is represented by its top/bottom interfaces and consequently requires that the slab be thin enough with respect to the wavelength of incident waves. Substituting equations (B6), (B7), and (B8) into equation (B5) and noting that each inner integral is a Fourier transform, we obtain

$$2Ck_z u(k_x, k_y, z) - iq(k_x, k_y, z + \Delta z) - 2k_0 F(k_x, k_y, z + \Delta z)$$

$$= \left(k_z u(k_x, k_y, z) + iq(k_x, k_y, z) + 2k_0 F(k_x, k_y, z) \right)$$

$$\times \exp(ik_z \Delta z). \quad (B9)$$

Equation (B9) is a wavenumber-domain wave equation that describes two-way wave propagation in the heterogeneous slab, including multiple forward- and backscatterings between Γ_0 and Γ_1. However, solving this equation requires operator deconvolution in the wavenumber domain because of the velocity-weighted wavefield $F(k_x, k_y, z + \Delta z)$.

For one-way wave propagation using the matching solution techniques, further simplification should be made to equation (B5) by reducing it to one-way version. From equation (B5), we see that two-way wave propagation involves two terms: the acoustic pressure $u(\mathbf{r})$ and acoustic pressure gradient $q(\mathbf{r})$. In practice, we do not often measure both $u(\mathbf{r})$ and $q(\mathbf{r})$ at a given level. The pressure gradient $q(\mathbf{r})$ at the slab entrance Γ_0 can be dropped by choosing Γ_0 as an acoustically soft boundary (Dirichlet boundary condition). This Rayleigh-type integral representation is valid if we neglect backscatterings. With this choice, no energy returns from the upper boundary Γ_0 and multiple reflections between Γ_0 and Γ_1 can be avoided, and equation (B9) is updated to

$$2Ck_z u(k_x, k_y, z) - iq(k_x, k_y, z + \Delta z) - 2k_0 F(k_x, k_y, z + \Delta z)$$

$$= (2k_z u(k_x, k_y, z) + 2k_0 F(k_x, k_y, z)) \exp(ik_z \Delta z). \quad (B10)$$

To account for the effect of transmission and refraction at Γ_1 on forward wave propagation, we need to build a boundary integral equation in the medium immediately below the slab

$$\frac{1}{2} u(\mathbf{r}) + \int_{\Gamma_1} \left[G(\mathbf{r}, \mathbf{r}') q(\mathbf{r}') + u(\mathbf{r}') \frac{\partial G(\mathbf{r}, \mathbf{r}')}{\partial n} \right] d\mathbf{r}' = 0. \quad (B11)$$

Applying the plane-wave representation of the Green's function to equation (B11) results in $iq(k_x, k_y, z + \Delta z) = -k_z' u(k_x, k_y, z + \Delta z)$, where k_z' is the wavenumber related to the medium immediately below Γ_1. Substituting in equation

(B10) gives

$$(2Ck_z + k'_z) u(k_x, k_y, z + \Delta z) - 2k_0 F(k_x, k_y, z + \Delta z)$$
$$= (2k_z u(k_x, k_y, z) + 2k_0 F(k_x, k_y, z)) \exp(ik_z \Delta z). \quad (B12)$$

This is one-way Lippmann–Schwinger wave equation accounts for the accumulated effect of both forward scattering by volume heterogeneities inside a slab and transmission/refraction between different slabs on wave amplitude and phase.

APPENDIX C

DISPERSION RELATION OF THREE-DIMENSIONAL BORN–KIRCHHOFF PROPAGATOR

This appendix further explores the physics of equation (B12), leading to several dispersion equations that correspond to some typical one-way propagators, including the Born–Kirchhoff (BK) propagator. These dispersion relations define the accuracy of one-way propagators.

To analyse the accuracy of equation (B12) in terms of acoustic refractive indices and propagation angles, we normalise the wavenumbers $\bar{k}_x = k_x/k_0$, $\bar{k}_y = k_y/k_0$, $\bar{k}_z = k_z/k_0$, and $\bar{k}'_z = k'_z/k'_0$ with k'_0, the reference wavenumber for the medium immediately below Γ_1. Taking $2k_z/(k_z + k'_z) \approx 1$ after Born approximation to the slab is reasonable. For convenience, we take the acoustic refractive index $n(\mathbf{r})$ of the slab as different constants n to avoid convolution operations in $F(k_x, k_y, z + \Delta z)$. Then, equation (B12) can be written as

$$u(k_x, k_y, z + \Delta z) \left[1 - \frac{ik_0 \Delta z O(n)}{2(\bar{k}_z + \bar{k}'_z)} \right]$$
$$= u(k_x, k_y, z) \left[1 + \frac{ik_z \Delta z O(n)}{2(\bar{k}_z + \bar{k}'_z)} \right] \exp(ik_z \Delta z). \quad (C1)$$

Since

$$\left| \frac{1 + \frac{ik_0 \Delta z O(n)}{2(\bar{k}_z + \bar{k}'_z)}}{1 - \frac{ik_0 \Delta z O(n)}{2(\bar{k}_z + \bar{k}'_z)}} \right| = 1,$$

equation (C1) becomes

$$u(k_x, k_y, z + \Delta z) = u(k_x, k_y, z) exp\left[i2 \arctan\left(\frac{k_0 \Delta z O(n)}{2(\bar{k}_z + \bar{k}'_z)} \right) \right]$$
$$\times \exp(ik_z \Delta z). \quad (C2)$$

Because of the Born approximation, we have

$$\tan\left[\frac{k_0 \Delta z O(n)}{2(\bar{k}_z + \bar{k}'_z)} \right] \approx \frac{k_0 \Delta z O(n)}{2(\bar{k}_z + \bar{k}'_z)},$$

which gives

$$u(k_x, k_y, z + \Delta z) = u(k_x, k_y, z) exp\left[\frac{ik_0 \Delta z O(n)}{(\bar{k}_z + \bar{k}'_z)} \right]$$
$$\times \exp(ik_z \Delta z). \quad (C3)$$

From equation (C3), we obtain the following Born dispersion relation:

$$\bar{k}_z = \sqrt{1 - \bar{k}_x^2 - \bar{k}_y^2}$$
$$+ \frac{n^2 - 1}{\sqrt{1 - \bar{k}_x^2 - \bar{k}_y^2} + \sqrt{1 - \bar{k}'^2_x - \bar{k}'^2_y}}. \quad (C4)$$

To make sense of this dispersion equation, we take $\bar{k}_x \approx \bar{k}'_x$, $\bar{k}_y \approx \bar{k}'_y$ and substitute it in equation (C4) to yield

$$\bar{k}_x^2 + \bar{k}_y^2 + \left(\bar{k}_z - \frac{0.5(n^2 - 1)}{\sqrt{1 - \bar{k}_x^2 - \bar{k}_y^2}} \right)^2 = 1. \quad (C5)$$

Here, $\bar{k}_z \approx \sqrt{1 - \bar{k}_x^2 - \bar{k}_y^2}$ for $n \approx 1$ (small perturbation) and $\bar{k}_z \approx 0.5(n^2 + 1)$ for $\bar{k}_x, \bar{k}_y \approx 0$ (small angle). Compared with the exact dispersion relation $\bar{k}_z = \sqrt{n - \bar{k}_x^2 - \bar{k}_y^2}$, we find that the Born approximation is a small perturbation approximation (fitting into its assumption) rather than a global small-angle approximation. It cannot remove the axial phase error, i.e., for $\bar{k}_x, \bar{k}_y \approx 0$, equation (C5) cannot arrive at exact values for any slowness perturbations except in the case $n = 1$. Figure C1 shows the poor performance of the Born dispersion equation (C5) for $n = 0.1 \sim 0.8$.

One can significantly improve the Born approximation by simplifying the relative slowness perturbation

$$O(n) = n^2 - 1 \approx 2(n - 1), \quad (C6)$$

which tends to smooth medium contrasts. Equation (C6) extends the Born dispersion relation (equation (C5)) to a more accurate form

$$\bar{k}_x^2 + \bar{k}_y^2 + \left(\bar{k}_z - \frac{n - 1}{\sqrt{1 - \bar{k}_x^2 - \bar{k}_y^2}} \right)^2 = 1. \quad (C7)$$

We see that $\bar{k}'_z \approx \sqrt{1 - \bar{k}_x^2 - \bar{k}_y^2}$ for $n \approx 1$ and $\bar{k}'_z \approx n$ for $\bar{k}_x, \bar{k}_y \approx 0$, which agrees with the exact dispersion relation.
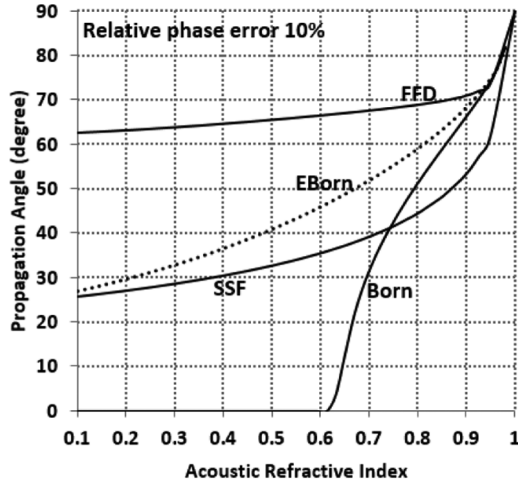
Figure C1 Comparison of angular spectra of several typical one-way propagators: Born, SSF, EBorn, and FFD Here, EBorn denotes the dispersion relation of the BK propagator.

Equation (C7) can be called the extended Born (EBorn) dispersion equation, and Fig. C1 demonstrates its significant improvement over the SSF approximation. We consider the simplification (equation (C6)) as refractive-index smoothing that extends the Born approximation to accommodate small propagation angles for arbitrarily strong-contrast media. Therefore, matching solution techniques based on equation (C7) would account for moderate perturbations and global small angles rather than the weak perturbations produced by the standard Born approximation. Despite its improved performance compared with the SSF approximation, one-way propagation by this improved Born dispersion relation (equation (C7)) using Fourier transforms is unstable because of the singularity obtained when $\bar{k}_x^2 + \bar{k}_y^2 \approx 1$ (large-angle waves). However, one-way propagation by its space-domain version (equation (6)) is unconditionally stable using diffraction summation. That is, equation (C7) is the dispersion relation of the BK propagator; this relation differs from the Kirchhoff propagator in that it accounts not only for the obliquity, spherical spreading, and wavelet shaping factors but also for the relative slowness perturbation in a laterally heterogeneous slab.

Applying the small-angle approximation $1/\sqrt{1 - \bar{k}_x^2 - \bar{k}_y^2} \approx 1$ to equation (C5) results in the so-called standard parabolic equation (Tappert 1977) with a dispersion relation of

$$\bar{k}_x^2 + \bar{k}_y^2 + (\bar{k}_z - 0.5(n^2 - 1))^2 = 1. \tag{C8}$$

Applying refractive-index smoothing (equation (C6)) to equation (C8) yields the following well-known split-step dispersion equation on which the current SSF method is based:

$$\bar{k}_x^2 + \bar{k}_y^2 + (\bar{k}_z - (n - 1))^2 = 1. \tag{C9}$$

From Fig. C1, we see that the small-angle approximation $1\sqrt{1 - \bar{k}_x^2 - \bar{k}_y^2} \approx 1$ decreases the benefit from the refractive-index smoothing and reduces the extended Born approximation to the SSF approximation.

With the above dispersion equations, Fourier matching algorithms using FFTs can be designed for one-way propagation in either moderate-contrast media or small propagation angles. For large to strong-contrast media, various hybrid methods that incorporate the FD scheme into the Fourier matching solutions have been proposed, theoretically permitting one-way propagation in arbitrary angles. These split-step FD solutions have been reported to allow larger grid spacings than pure FD methods. For instance, the split-step FD propagator (Thomson 1990), the split-step Padé solution (Collins 1993), and the FFD propagator (Ristow and Rühl 1994) are of the same form with the rational approximation

$$\bar{k}_z = \sqrt{1 - \bar{k}_x^2 - \bar{k}_y^2} + n - 1 + \sum_{j=1}^{m} \frac{a_j(n)\left(\bar{k}_x^2 + \bar{k}_y^2\right)}{1 + b_j(n)\left(\bar{k}_x^2 + \bar{k}_y^2\right)}, \tag{C10}$$

with coefficients varying with n. We see that these split-step FD propagators hierarchically consist of the reference phase-shift solution (the first term), the split-step correction term (the second term), and a parabolic correction term (the last term). Cross-coupling of $\bar{k}_x$, $\bar{k}_y$, and n in the last term shows that equation (C10) is not a degenerate operator expression and consequently requires an extra implicit FD implementation.